J. Fluid Mech. (2007), *vol.* 583, *pp.* 423–442. © 2007 Cambridge University Press
doi:10.1017/S0022112007006313 Printed in the United Kingdom

Three-dimensional shock tube flows for dense gases

ALBERTO GUARDONE

Dipartimento di Ingegneria Aerospaziale, Politecnico di Milano,
Via La Masa 34, 20156 Milano, Italy

(Received 1 August 2006 and in revised form 6 March 2007)

The formation process of a non-classical rarefaction shock wave in dense gas shock tubes is investigated by means of numerical simulations. To this purpose, a novel numerical scheme for the solution of the Euler equations under non-ideal thermodynamics is presented, and applied for the first time to the simulation of non-classical fully three-dimensional flows. Numerical simulations are carried out to study the complex flow field resulting from the partial burst of the shock tube diaphragm, a situation that has been observed in preliminary trials of a dense gas shock tube experiment. Beyond the many similarities with the corresponding classical flow, the non-classical wave field is characterized by the occurrence of anomalous compression isentropic waves and rarefaction shocks propagating past the leading rarefaction shock front. Negative mass flow through the rarefaction shock wave results in a limited interaction with the contact surface close to the diaphragm, a peculiarity of the non-classical regime. The geometrical asymmetry does not prevent the formation of a single rarefaction shock front, though the pressure difference across the rarefaction wave is predicted to be weaker than the one which would be obtained by the complete burst of the diaphragm.

1. Introduction

The gasdynamics of a fluid operating in a thermodynamic region near to or overlapping liquid–vapour equilibrium may significantly differ from that of dilute gases from both a qualitative and quantitative point of view. The presence of well-known thermodynamic processes such as liquid–vapour transition or critical-point phenomena may lead to the appearance of 'exotic' wave fields including rarefaction shocks, mixed, composite and split waves, as reviewed by Menikoff & Plohr (1989). For example, mixed and split waves may form when the flow undergoes a phase transition, see, for instance, Bethe (1942). These waves are indicated as *non-classical waves*, to be contrasted with compression shock waves and rarefaction isentropic waves usually encountered in (classical) gasdynamics, see Cramer & Kluwick (1984). In particular, non-classical rarefaction shocks are referred to as *negative shock waves* and are thermodynamically admissible provided that the *fundamental derivative of gasdynamics* Γ of Thompson (1971) becomes negative. Γ is defined as follows

$$\Gamma(s, v) = -\frac{v}{2}\left(\frac{\partial^2 P}{\partial v^2}\right)_s \Big/ \left(\frac{\partial P}{\partial v}\right)_s = \frac{v^3}{2c^2}\left(\frac{\partial^2 P}{\partial v^2}\right)_s, \tag{1.1}$$

where s is the specific (per unit mass) entropy, v is the specific volume, P is the pressure and c is the speed of sound. Note that for a polytropic, i.e. constant specific heats,

https://doi.org/10.1017/S0022112007006313 Published online by Cambridge University Press

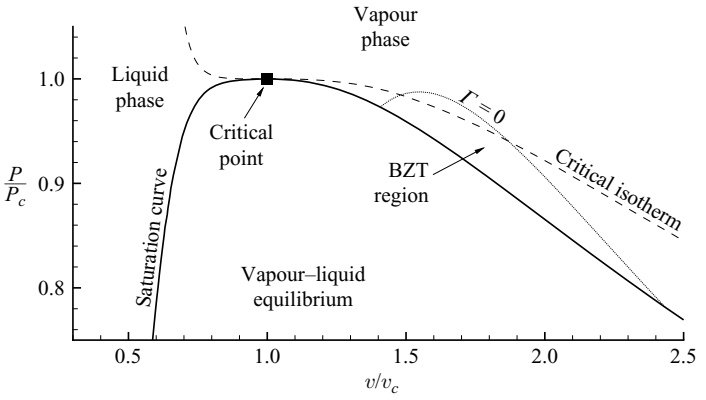

FIGURE 1. Saturation curve and critical isotherm for fluid PP10. The non-classical BZT region is bounded by the $\Gamma = 0$ line and the vapour side of the saturation curve. Thompson & Lambrakis (1973) noticed that the BZT region is sufficiently far from the liquid–vapour critical point for critical phenomena to be negligible.

ideal gas, $\Gamma = (\gamma + 1)/2 = \text{const}$, with $\gamma = c_P/c_v$ being the ratio of the specific heats at constant pressure and volume. Since $\gamma > 1$, namely, $c_P > c_v$, for thermodynamic stability, negative values of Γ are not possible for the so-called perfect gases.

Non-classical behaviour in flows displaying liquid–vapour phase transition has been observed experimentally by Thompson, Carofano & Kim (1986). Ivanov & Novikov (1961) reported non-classical wave fields in allotropic phase changes in a steel specimen. Bethe (1942) and Weyl (1949) speculated on the possibility for real fluids to exhibit non-classical gasdynamic phenomena in the single-phase vapour region. By using the simple polytropic van der Waals model, they discovered that molecularly complex vapours may allow for non-classical gasdynamic phenomena to occur in a thermodynamic region located in the vicinity of the liquid–vapour saturation curve (figure 1), see also Zel'dovich (1946) and Hayes (1960). Thompson (1971), Cramer (1989), Colonna & Silva (2003) and Guardone & Argrow (2005) investigated the existence of a $\Gamma < 0$ region for different fluids, using more accurate thermodynamic models. A number of molecularly complex hydrocarbons, perfluorocarbons and siloxanes have been identified which should exhibit a $\Gamma < 0$ region in the vapour phase. These fluids are usually called BZT vapours after Bethe, Zel'dovich and Thompson. No experimental evidence of the existence of non-classical phenomena in the vapour phase is available. Borisov *et al.* (1983) claimed to have observed a negative shock wave in Freon-13. The interpretation of these results was challenged among others by Fergason *et al.* (2001) and the observed wave field is now believed to be related to both critical-point and two-phase effects.

A novel shock tube experiment has been designed and tested at the University of Colorado at Boulder with the aim of providing an experimental proof of the occurrence of non-classical gasdynamic behaviour in fluid PP10 ($C_{13}F_{22}$). Preliminary results using nitrogen gas (Fergason, Guardone & Argrow 2003) pointed to the shock tube diaphragm manufacturing and operation as critical issues related to the experimental set-up and motivate the present study. In particular, the imperfect burst of the shock tube diaphragm was found to introduce significant three-dimensional disturbances in the flow field, which possibly prevent an indisputable detection of non-classical phenomena. A similar experimental facility is currently under construction at the Delft University of Technology, the Netherlands, in collaboration with the Politecnico di Milano and the University of Brescia, Italy (see Zamfirescu,

https://doi.org/10.1017/S0022112007006313 Published online by Cambridge University Press

Guardone & Colonna 2006). The adopted solution includes a fast opening valve, to guarantee repeatability and complete clearance. As the valve is opened, the fluid in the high-pressure tube flows into the low-pressure reservoir through a nozzle. The proposed Ludwieg tube-like design uses siloxanes – silicone oils currently used also in organic Rankine cycle engines – as working fluids.

In both experiments, a rarefaction shock wave is expected to form as the shock tube diaphragm/fast opening valve opens and its propagation velocity is to be measured by means of wall-mounted pressure transducers: if the wave speed is greater than the local speed of sound in the unperturbed medium, then the rarefaction wave is indeed a non-classical rarefaction shock wave moving at supersonic speed. The understanding of the formation process of the rarefaction shock front is therefore key to the correct design of the experimental apparatus and to a conclusive interpretation of the measurements.

The formation of a single shock front resulting from the partial and/or not instantaneous opening of the diaphragm in classical flows has been the subject of a number of studies, since significant multidimensional effects occur close to the diaphragm location (see e.g. Glass & Sislian 1994; Petrie-Repar & Jacobs 1998), and past the shock itself (see Persico, Gaetani & Guardone 2005). However, shock tube flows of dense gases are usually qualitatively very different from their classical, namely, perfect gas, counterparts (see Argrow 1996; Guardone & Vigevano 2002; Guardone, Vigevano & Argrow 2004 and Brown & Argrow 1997 for one- and two-dimensional non-classical shock tube flows, respectively). As a consequence, the formation process of a rarefaction shock front is expected to present significant differences with respect to the classical case.

The investigation of the non-classical phenomena associated with the formation of a rarefaction shock wave is the focus of the present work. As an example, the flow field past a partially opened diaphragm is considered, since it represents a challenging situation and it is also motivated by the first experimental observations in the Boulder experiment. To investigate the spatially complex non-classical wave field occurring in the real shock tube experiment, a numerical scheme for the solution of the three-dimensional Euler equations is outlined and used here to simulate the three-dimensional flow occurring in the Boulder shock tube apparatus.

The paper is structured as follows. In § 2, the Euler equations governing inviscid flows of real gases are briefly recalled and the thermodynamic model of the fluid is presented. The discrete form of the Euler equations for non-ideal gases is then obtained by means of an edge-based finite-volume scheme. To comply with the need to include complex non-ideal thermodynamic models, the Roe linearization technique proposed by Guardone & Vigevano (2002) for the polytropic van der Waals model is generalized here to a fully arbitrary thermodynamic model, as detailed in § 3. In § 4, the proposed method is applied to the simulation of the shock tube flow resulting from the partial burst of the diaphragm. Results include dilute gas classical computations and the simulation of the non-classical dense gas shock tube experiment. To the author's knowledge, the results presented here are the first three-dimensional simulations of non-classical wave fields.

2. Governing equations

The conservative form of the three-dimensional Euler equations of gasdynamics of interest here, is

$$\frac{\partial u}{\partial t} + \nabla \cdot \boldsymbol{f}(u) = 0, \tag{2.1}$$

https://doi.org/10.1017/S0022112007006313 Published online by Cambridge University Press

where u, $u = (\rho, \boldsymbol{m}, E^t)^T \in \mathbb{R}^+ \times \mathbb{R}^4$, is the vector unknown of the mass density ρ, momentum density vector $\boldsymbol{m}$ and total energy per unit volume E^t, $\boldsymbol{f}(u)$, $\boldsymbol{f} \in \mathbb{R}^5 \times \mathbb{R}^3$, is the flux function and where it is understood that $\nabla \cdot \boldsymbol{f} = \partial f_x/\partial x + \partial f_y/\partial y + \partial f_z/\partial z$, with f_x, f_y, $f_z \in \mathbb{R}^5$ being the 'Cartesian components' of the flux function $\boldsymbol{f}$. The solution of (2.1) is sought for in the spatial domain $\Omega \in \mathbb{R}^3$, with boundary $\partial\Omega$ for all times $t \in \mathbb{R}^+$. System (2.1) is made complete by specifying suitable initial and boundary conditions (see e.g. Godlewski & Raviart 1994). The flux function $\boldsymbol{f}(u)$ is defined as

$$\boldsymbol{f}(u) = \left(\boldsymbol{m}, \frac{\boldsymbol{m} \otimes \boldsymbol{m}}{\rho} + \Pi(u)\, \boldsymbol{I}, \ [E^t + \Pi(u)] \frac{\boldsymbol{m}}{\rho} \right)^T, \tag{2.2}$$

where $\boldsymbol{I}$ is the 3×3 identity matrix. From the pressure equation of state $P = P(e, \rho)$, e being the internal energy per unit mass, the following *pressure function* $\Pi(u)$ in terms of the conservative variables,

$$\Pi(u) = P\left(\frac{E^t}{\rho} - \frac{1}{2}\frac{|\boldsymbol{m}|^2}{\rho^2}, \ \rho \right), \tag{2.3}$$

has been introduced. The thermodynamic information required to write the pressure equations of state $P(e, \rho)$ can be obtained by specifying for example the two (compatible) equations of state for the pressure $P = P(T, v)$ and for the internal energy $e = e(T, v)$ as a function of the temperature T and the specific volume v; together, these equations of state define a complete thermodynamic model (Callen 1985). For example, for a polytropic ideal gas, we have $P(T, v) = RT/v$ and $e(T, v) = e_{ref} + R(T - T_{ref})/(\gamma - 1)$, with $R = \mathscr{R}/M$, $\mathscr{R}$ being the universal gas constant and M the molecular weight, and where e_{ref} and T_{ref} are the values of the energy and the temperature in an arbitrary reference state. Hence, $P(e, \rho) = \rho\,[(\gamma - 1)(e - e_{ref}) + RT_{ref}]$.

In the computations, the Martin–Hou pressure equation of state (Martin & Hou 1955; Martin, Kapoor & De Nevers 1958) has been selected for its suitability in modelling fluorinated substances near the liquid-vapour saturation curve (Cramer 1989; Emanuel 1994; Guardone *et al.* 2004). The complete Martin–Hou model is given by the following two equations of state

$$P(T, v) = \frac{RT}{v - b} + \sum_{i=2}^{5} \frac{Q_i(T)}{(v - b)^i}, \tag{2.4}$$

$$e(T, v) = e_{ref} + \int_{T_{ref}}^{T} c_{v_\infty}(\tau)\, \mathrm{d}\tau - \sum_{i=2}^{5} \frac{T\, Q_i'(T) - Q_i(T)}{(i - 1)(v - b)^{i-1}}, \tag{2.5}$$

where $Q_i(T) = A_i + B_i T + C_i \exp(-kT/T_c)$, $k = 5.475$ and $Q_i'(T) = \mathrm{d}Q_i(T)/\mathrm{d}T$. The gas-dependent coefficients b, A_i, B_i and C_i have been obtained by applying the approximate procedure of Cramer (1989), which requires the specification of the critical-point coordinates and the boiling temperature T_b at 1 atm. These data are reported in § 4 for air and fluid PP10. In the expression of the energy equation of state, the function $c_{v_\infty}(T)$ is the specific heat at constant volume in the dilute gas limit or, more precisely,

$$c_{v_\infty}(T) = \lim_{v \to \infty} c_v(T, v),$$

where $c_v(T, v) = \partial e(T, v)/\partial T$ is the specific heat at constant volume. Following Thompson & Lambrakis (1973), the function $c_{v_\infty}(T)$ is approximated in the

https://doi.org/10.1017/S0022112007006313 Published online by Cambridge University Press

neighbourhood of the critical point by the power law

$$c_{v_\infty}(T) = c_{v_\infty}(T_c)\left(\frac{T}{T_c}\right)^n, \tag{2.6}$$

with T_c critical temperature. The values of $c_{v_\infty}(T_c)$ and n are given by Lambrakis & Thompson (1972) and Cramer (1989) for several molecularly complex fluids.

Differently from the polytropic ideal gas, the analytical expression for the pressure equation of state $P = P(e, \rho)$ is not easily obtained in the case of the Martin–Hou gas model. The evaluation of the pressure function Π is therefore performed numerically in two steps. First, the value of the temperature is computed from the vector variable u by solving for T the nonlinear equation

$$\phi(T, u) = e(T, 1/\rho) - e(u) = 0,$$

with $e(u) = E^t/\rho - (|\boldsymbol{m}|/\rho)^2/2$; the equation above being actually the implicit definition of the function $T = T(u)$. Newton iteration requires us to know the function $e(T, v)$ and its partial derivative with respect to T. In the computations, the ideal polytropic approximation is used to provide the initial guess for the Newton scheme, namely, $T_{guess} = T_{ref} + (e - e_{ref})/c_{v_\infty}(T_c)$. Afterward, the pressure is computed from the equation of state (2.4) as $\Pi(u) = P(T(u), 1/\rho)$.

As a final remark, it should be recalled that no thermodynamic data are available to assess the accuracy of the Martin–Hou thermodynamic model of fluid PP10, as discussed by Guardone *et al.* (2004). In particular, uncertainties in the predictions of the critical point and on the dilute gas specific heat may result in large uncertainties in the determination of the value of Γ. Moreover, it is well known that the accuracy of the Martin–Hou model is very poor close to the saturation curve at low pressure ($P < 0.6\, P_c$). This is, however, not the case for the dilute ($v \gg v_c$) and dense ($P \simeq P_c$) gas computations carried out in the present work.

3. Numerical method

Standard numerical techniques for solving the Euler equations for classical gasdynamics may be unsuitable for the simulation of non-classical waves in the BZT regime, as pointed out, for instance, by Menikoff & Plohr (1989) and Rider & Bates (2001). To overcome these difficulties, an extension to the Roe linearization technique of Guardone & Vigevano (2002) for the polytropic van der Waals gas is derived to compute non-classical flows of Martin–Hou vapours. The approximate Riemann solver is included into an edge-based node-centred finite-volume scheme for unstructured grids. The main features of the numerical scheme are now briefly recalled and the Roe linearization procedure for a general thermodynamic model is detailed.

Following Selmin (1993), the discrete form of the governing equations (2.1) is obtained here by applying the node-centred finite-volume method for unstructured grids. A high-resolution expression for the integrated numerical flux is then obtained by resorting to the total variation diminishing (TVD) approach, in which the centred second-order approximation of the numerical fluxes is replaced by the first-order scheme of Roe (1981) near flow discontinuities. The switch is controlled by the flux limiter function of van Leer (1974). The fully discrete form of (2.1) is finally obtained by time discretization via the total variation bounded (TVB) multistage scheme of Shu (1988). Slip boundary conditions are applied at the shock tube solid boundaries.

https://doi.org/10.1017/S0022112007006313 Published online by Cambridge University Press

The Roe matrix $\widetilde{A}$, $\widetilde{A} \in \mathbb{R}^5 \times \mathbb{R}^5$, which is required to compute the first-order upwind integrated numerical fluxes, is constructed according to the following prescription given by Roe (1981)

$$\text{(i) Conservation:} \quad \widetilde{A}[u_k - u_i] = [\boldsymbol{f}(u_k) - \boldsymbol{f}(u_i)] \cdot \boldsymbol{\eta}_{ik}, \tag{3.1a}$$

$$\text{(ii) Consistency:} \quad \widetilde{A} \to \boldsymbol{A}(u) \cdot \boldsymbol{\eta}_{ik} \quad \text{as} \quad u_i, u_k \to u, \tag{3.1b}$$

(iii) Hyperbolicity: $\widetilde{A}$ has real eigenvalues and a corresponding set of eigenvectors that form a basis in $\mathbb{R}^5$,

where indexes i and k indicate grid nodes belonging to a grid edge crossing the interface between the ith and the kth finite-volume cells, and where $\boldsymbol{\eta}_{ik}$ is the integrated normal over interface ik. The Roe matrix is chosen here to be in Jacobian form, namely,

$$\widetilde{A} = \boldsymbol{A}(\tilde{u}) \cdot \boldsymbol{\eta}_{ik}, \tag{3.2}$$

where $\boldsymbol{A}$, $\boldsymbol{A}(u) = \partial \boldsymbol{f}(u)/\partial u$, is the Jacobian matrix of the flux $\boldsymbol{f}(u)$ to be evaluated in some suitable intermediate state $\tilde{u}$. The Roe intermediate state $\tilde{u}$ is therefore obtained by solving the following 5×5 system

$$[\boldsymbol{A}(\tilde{u}) \cdot \boldsymbol{\eta}_{ik}]\,(u_k - u_i) = [\boldsymbol{f}(u_k) - \boldsymbol{f}(u_i)] \cdot \boldsymbol{\eta}_{ik},$$

for the five unknown components of $\tilde{u}$, namely, condition (i). Correspondingly, condition (ii) simplifies to $\tilde{u}(u_i, u_k) \to u$ as $u_i, u_k \to u$ and (iii) is identically satisfied for any choice of the intermediate state $\tilde{u} \in \mathbb{R}^+ \times \mathbb{R}^4$. From rotational invariance of the Euler equations (see e.g. Godlewski & Raviart 1994, p. 321), it follows that the intermediate state $\tilde{u}$ does not depend on the direction vector $\boldsymbol{\eta}_{ik}$ and therefore $\tilde{u} = \tilde{u}(u_i, u_k)$. Guardone & Vigevano (2002) showed that the celebrated average of Roe (1981) for ideal polytropic gases, namely,

$$\widetilde{\boldsymbol{w}} = \frac{\sqrt{\rho_i}\,\boldsymbol{w}_i + \sqrt{\rho_k}\,\boldsymbol{w}_k}{\sqrt{\rho_i} + \sqrt{\rho_k}}, \qquad \widetilde{h^t} = \frac{\sqrt{\rho_i}\,h_i^t + \sqrt{\rho_k}\,h_k^t}{\sqrt{\rho_i} + \sqrt{\rho_k}},$$

where $\boldsymbol{w}$, $\boldsymbol{w} = \boldsymbol{m}/\rho$ is the velocity vector and h^t, $h^t = h + |\boldsymbol{w}|^2/2$ is the total specific enthalpy, remains valid also in the case of non-ideal thermodynamic models provided that the intermediate density $\widetilde{\rho}$ is found as the solution of the following system

$$\left.\begin{aligned} &h(\widetilde{E}, \widetilde{\rho}) = \widetilde{h^t} - \tfrac{1}{2}|\widetilde{\boldsymbol{w}}|^2, \\ &\kappa(\widetilde{E}, \widetilde{\rho})\,\Delta E + \chi(\widetilde{E}, \widetilde{\rho})\,\Delta\rho = \Delta P, \end{aligned}\right\} \tag{3.3}$$

of two equations in the two unknowns: intermediate density $\widetilde{\rho}$ and intermediate internal energy density $\widetilde{E}$. The operator Δ indicates state differences, namely, $\Delta(\cdot) = (\cdot)_k - (\cdot)_i$. In the system above, the specific enthalpy h is computed from its definition, $h(E, \rho) = [E + P(E, \rho)]/\rho$ and the functions κ and χ are the partial derivatives of the pressure equation of state $P = P(E, \rho)$, namely

$$\kappa = \left(\frac{\partial P}{\partial E}\right)_{\rho}, \qquad \chi = \left(\frac{\partial P}{\partial \rho}\right)_{E}. \tag{3.4}$$

For a polytropic van der Waals gas, (3.3) reduces to a single third-order algebraic equation for the intermediate density $\widetilde{\rho}$ and can be solved analytically using standard solution formula (Guardone & Vigevano 2002). For more complex

https://doi.org/10.1017/S0022112007006313 Published online by Cambridge University Press

thermodynamic models, the solution of (3.3) requires numerical techniques (Guardone 2001).

In the present study, an iterative Newton method is used to solve (3.3). The computation of the pressure $P = P(E, \rho)$ at each iteration of the Newtonian scheme would be computationally expensive since an explicit analytical expression is usually not available for complex thermodynamic models and hence its evaluation would require inner iterations. To avoid that, the solution of (3.3) is sought for the new variables, intermediate temperature $\widetilde{T}$ and specific volume $\widetilde{v}$, since the specific enthalpy is computed immediately from the equations of state as $h(T, v) = e(T, v) + v\,P(T, v)$. From the theorem of chain derivatives, we have

$$\kappa(T, v) = v \left(\frac{\partial P}{\partial T}\right)_v \Big/ \left(\frac{\partial e}{\partial T}\right)_v,$$
$$\chi(T, v) = -v^2 \left(\frac{\partial P}{\partial v}\right)_T + v \left(\frac{\partial P}{\partial T}\right)_v \left[v \left(\frac{\partial e}{\partial v}\right)_T - e\right] \Big/ \left(\frac{\partial e}{\partial T}\right)_v,$$

which allows for (3.3) to be recast in terms of $\widetilde{T}$ and $\widetilde{v}$ only as

$$\left.\begin{aligned} &h(\widetilde{T}, \widetilde{v}) = \widetilde{h^t} - \tfrac{1}{2}|\widetilde{\boldsymbol{w}}|^2, \\ &\kappa(\widetilde{T}, \widetilde{v})\,\Delta E + \chi(\widetilde{T}, \widetilde{v})\,\Delta\rho = \Delta P. \end{aligned}\right\} \tag{3.5}$$

Solution of (3.5) is obtained by means of a Newton algorithm; fewer than five iterations are usually required for convergence using as the initial guess for the Newton solver the algebraic mean of the value of the unknowns at nodes i and k. The intermediate state of the conservative variables appearing in the definition of the Roe matrix (3.2) is finally obtained as

$$\tilde{u} = \tilde{u}(\widetilde{T}, \widetilde{v}, \widetilde{\boldsymbol{w}}) = \frac{1}{\widetilde{v}}\,(1, \widetilde{\boldsymbol{w}}, e(\widetilde{T}, \widetilde{v}) + \tfrac{1}{2}|\widetilde{\boldsymbol{w}}|^2)^T.$$

In the computations, the entropy fix of Harten & Hyman (1983), whose suitability for non-classical flows is discussed by Guardone & Vigevano (2002), has been used to fulfil the entropy condition.

4. Build-up of a nonclassical rarefaction shock wave

The proposed numerical scheme is applied to the computation of three-dimensional shock tube flows of dense gases. In § 4.1, the incomplete opening of a shock tube diaphragm for air in dilute gas conditions is first studied, to gain further confidence in the numerical solution procedure. Numerical results are verified against experimental data. In § 4.2, the Boulder non-classical shock tube experiment is briefly described and the fully three-dimensional non-classical flow field resulting from the partial burst of the diaphragm is investigated numerically to study the formation process of a rarefaction shock front.

4.1. *Recovery of perfect gas results*

The shock tube flow resulting from the incomplete opening of the shock tube diaphragm is now studied for air in dilute gas conditions and at room temperature. The purpose of the present section is two-fold. On the one hand, numerical results are compared to experimental data to assess the correctness of the proposed methodology and to verify the consistency of the thermodynamic model, which is expected to reproduce the dilute gas state with high accuracy. On the other hand, this preliminary

https://doi.org/10.1017/S0022112007006313 Published online by Cambridge University Press

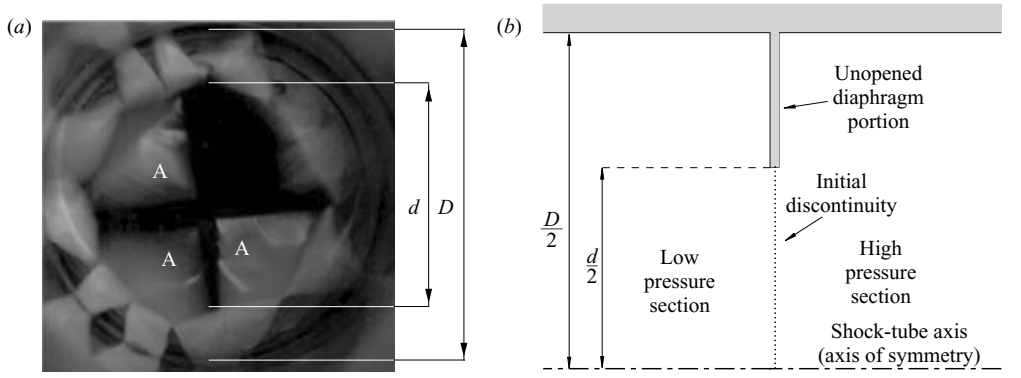

FIGURE 2. (*a*) Incomplete diaphragm burst in dilute air. D is the diameter of the diaphragm, namely, the inner diameter of the shock tube; d is the diameter of the opened portion of the diaphragm. Note the pre-cut aluminium plates on the high-pressure side of the diaphragm, labelled A. From high-speed camera recording, the plates are seen not to introduce a significant blockage during operations (see Persico *et al.* 2005). (*b*) Axisymmetric computational domain near the diaphragm location. Initial data are discontinuous across the diaphragm section.

study is necessary to evaluate the suitability of two relevant assumptions which also hold in the simulations of dense gas shock tube flow fields. The first hypothesis is that the wave propagation process and the intensity of the shock wave are affected only negligibly by viscous stresses and thermal conductivity, that is, that the Euler equations for an inviscid compressible fluid with zero thermal conductivity are adequate for predicting the shock dynamics. Moreover, in the following it is assumed that the effects of the diaphragm dynamics are significant only close to the diaphragm section, that is, that sufficiently far from the diaphragm, the wave pattern does not depend on the spatial and temporal details of the diaphragm dynamics. Accordingly, the diaphragm is assumed to be partially but instantaneously opened at the beginning of the simulations, to avoid resorting to complex mathematical models including the fluid interaction with a rapidly deforming diaphragm.

In the shock tube experiment Persico *et al.* (2005), a nearly axisymmetric petalling of the diaphragm (figure 2*a*), is observed and the incomplete burst of the diaphragm is studied to investigate its influence on the shock tube performance as a calibrating device for fast-response pressure probes. The pressure difference across the diaphragm is less than 1 atm, which is similar to the dense gas case to be studied in the next section.

The shock tube has a total length of 6.5 m and an internal diameter of 80 mm. The high-pressure section (1.5 m long) and the low-pressure section (5 m long, open to the ambient pressure) are separated by a 0.1 mm thick diaphragm made of DCfix^{TM} plastic. To avoid uneven tearing of the diaphragm and to increase the stiffness of the plastic membrane, four aluminium plates with a thickness of 0.08 mm are glued onto the side of the diaphragm facing the high-pressure section (figure 2*a*). The diaphragm bursting process is studied by means of a high-speed camera to estimate the total opening time of the diaphragm, which is about 350 µs. In nominal conditions, the diaphragm opens to clear a circular section with diameter of about 55–60 mm, that is 70–75% of the internal tube diameter. Further details on the experimental set-up and on the instrumentation are given by Persico *et al.* (2005).

To reduce the computational effort, the shock tube is described by the axisymmetric geometry shown in figure 2. The axisymmetric version of the code is run on an

https://doi.org/10.1017/S0022112007006313 Published online by Cambridge University Press

Section	v/v_c	P/P_c	T/T_c	v ($m^3\ kg^{-1}$)	P (atm)	T (K)	Γ
High pressure	139.8	0.05033	2.232	0.4475	1.872	295.8	1.202
Low pressure	262.5	0.02681	2.232	0.8400	0.9973	295.8	1.202

TABLE 1. Initial conditions for the reference shock tube problem under the polytropic Martin–Hou model for air. The molecular weight M is 28.966 kg m^{-3}. The critical point for air reported by Perry & Green (1984) is $P_c = 37.2$ atm, $T_c = 132.45$ K, $v_c = 0.0032$ kg m^{-3} and the boiling temperature at 1atm is $T_b = 80$ K. The (constant) specific heat ratio $\gamma = c_P/c_v$ is 1.402.

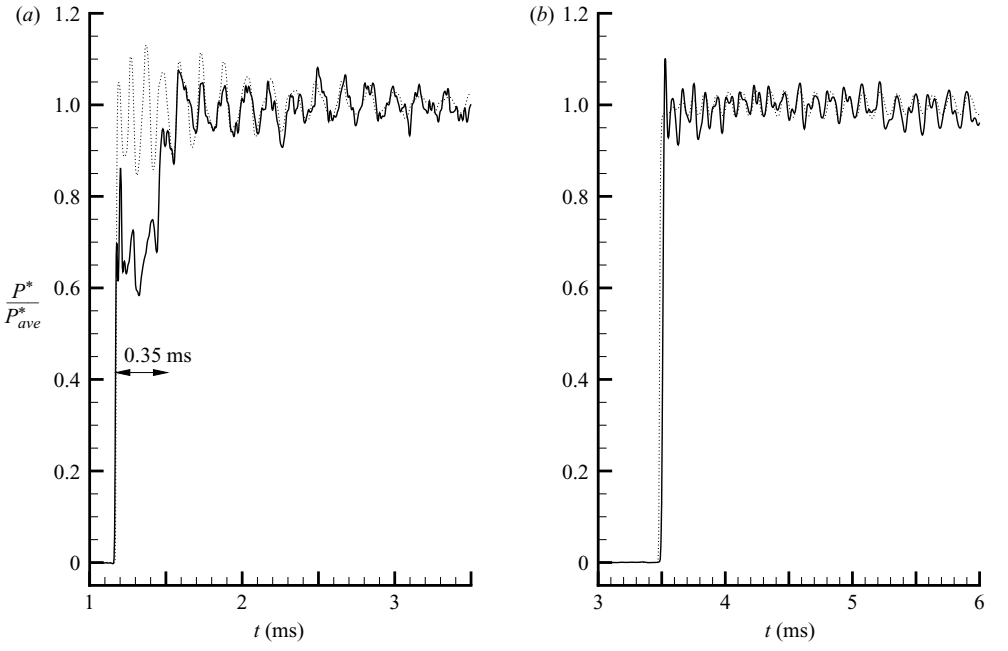

FIGURE 3. Numerical simulation for the partial axisymmetric burst of the diaphragm (. . .) and experimental results for air in dilute conditions (——). Initial gas state conditions are given in table 1. Results refer to the gauge total pressure P^* measured by probes 1 (*a*) and 2 (*b*), located 450 mm (5.625 D, where D is the shock tube diameter) and 1650 mm (20.625 D) downwind of the diaphragm position, respectively. P^*_{ave} is the average post-shock gauge total pressure.

unstructured grid made of 122 605 triangles (63 944 nodes). Initial conditions for the numerical tests are given in table 1, where the relevant data for applying the Martin–Hou model to air are also given.

Numerical results and experimental values for the total pressure are compared at two measurement stations on the axis of symmetry located 450 mm (5.625 D, where D is the shock tube diameter) and 1650 mm (20.625 D) downwind of the diaphragm position, respectively. The agreement between numerical and experimental results is fairly good (figure 3) in terms of average post-shock pressure and of the frequency of post-shock pressure oscillations, except for the probe closest to the diaphragm section. In this case, the initial portions of the numerical and experimental signals differ significantly for a time span comparable to the diaphragm opening time of 0.35 ms.

https://doi.org/10.1017/S0022112007006313 Published online by Cambridge University Press

Section	v/v_c	P/P_c	T/T_c	v ($m^3\ kg^{-1}$)	P (atm)	T (K)	Γ
High pressure	1.5572	0.96988	0.99819	2.493×10^{-3}	15.497	631.00	−0.11715
Low pressure	2.49761	0.84124	0.99819	3.998×10^{-3}	13.443	631.00	0.29220

TABLE 2. Initial conditions for the three-dimensional shock tube problem under the non-polytropic Martin–Hou model for PP10, from Fergason (2001). From manufacturer data, the critical-point parameters for fluid PP10 are as follows: molecular weight $M = 574\,kg\,m^{-3}$, critical temperature $T_c = 630.15$ K, critical pressure $P_c = 16.2$ atm and critical compressibility factor $Z_c = P_c v_c/(RT_c) = 0.2859$, with v_c critical volume. The boiling temperature at 1 atm is $T_b = 467$K. The dimensionless ideal specific heat and the non-polytropic exponent in (2.6) are $c_{v_\infty}(T_c)/R = 78.37$ and $n = 0.5255$, respectively, (see Cramer 1989).

This discrepancy is believed to be related to the diaphragm dynamics, which is not modelled in the simulations, and it is not relevant at measurement stations located further downstream, where a single shock front is present and the information related to the shock building process has been destroyed. The numerical results shown in figure 3 are indistinguishable from those of Persico *et al.* (2005), based on an ideal polytropic description of air.

The numerical model is therefore deemed to compute correctly shock tube flows resulting from the incomplete burst of the diaphragm, in terms of both thermodynamic consistency in the dilute gas limit and correctness of the aforementioned simplifying assumptions regarding the influence of the details of the diaphragm dynamics in the far field.

4.2. *Non-classical shock tube simulations*

In the present section, the formation process of a single rarefaction shock front in shock tube flows is studied by means of numerical simulations. As an example of this kind of flow, the dense shock tube experiment of Fergason (2001) and Fergason *et al.* (2003) is considered. The shock tube is made from Type 304, 4 in, Schedule 80 stainless steel tubing, with internal diameter $D = 9.718$ cm. The 4.88 m long tube is completely contained within heating elements to maintain a uniform temperature in both the high- and low-pressure sections. The diaphragm is a 0.1 mm thick copper sheet scored with a cross pattern for a rapid even burst and it is located 3.04 m from the end of the high-pressure section. The dense gas shock tube is designed to use the same fluid in the driver and driven sections to avoid complex fluid separation systems.

For suitable initial conditions, see Fergason (2001) and Fergason *et al.* (2001). A triple-discontinuity wave field in fluid PP10 is expected to form, with a classical compression shock wave (CSW) and a contact surface (CS) moving towards the low-pressure side of the shock tube together and a non-classical rarefaction shock wave (RSW), completely embedded in the non-classical region, moving towards the high-pressure region. In figure 4, the triple-discontinuity flow field is computed starting from the initial conditions summarized in table 2, where relevant thermodynamic properties of fluid PP10 are also given, and assuming an instantaneous and complete burst of the shock tube diaphragm. Note that the present initial conditions have been computed by using the Martin–Hou model of fluid PP10, whose accuracy in determining the thermodynamic properties of dense gases remains questionable (Guardone *et al.* 2004).

https://doi.org/10.1017/S0022112007006313 Published online by Cambridge University Press

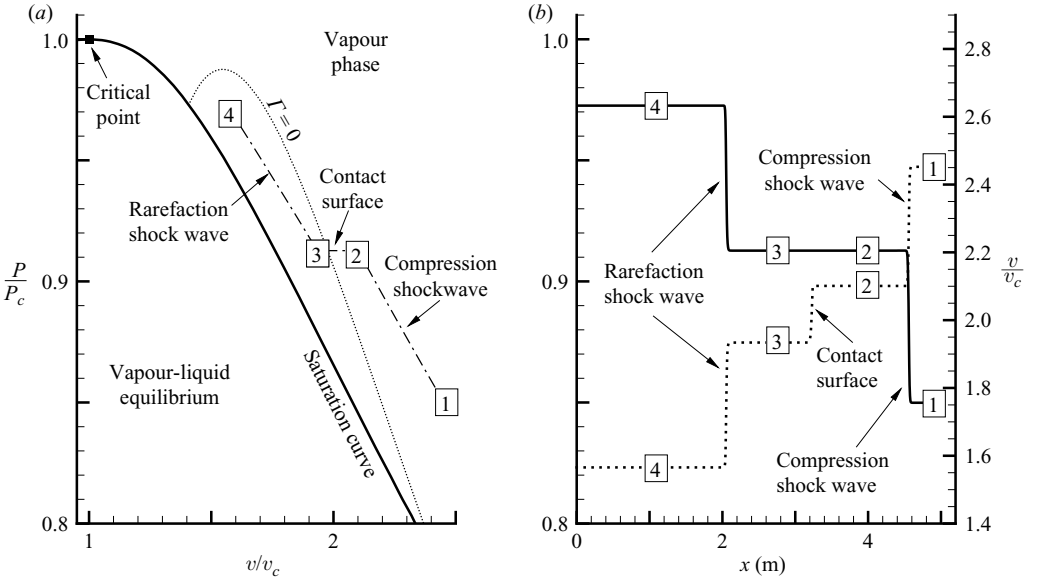

FIGURE 4. One-dimensional numerical solution of the triple-discontinuity shock tube problem under the non-polytropic Martin–Hou model for fluid PP10. States 4 and 1 are the initial state in the high- and low-pressure sections, respectively, see table 2. (*a*) Solution in the (v, P)-plane together with the saturation curve and the $\Gamma = 0$ locus. (*b*) —, reduced pressure P/P_c and . . ., specific volume v/v_c along the shock tube at time $t = 29.46$ ms. The diaphragm is located at $x_{diaph} = 3$ m.

In the high-pressure side of the shock tube, close to its endwall, namely, at $x_A/D = 25.1$ (2.44 m) and $x_B/D = 28.5$ (2.77 m) from the diaphragm, two static pressure transducers A and B are positioned on the tube surface to measure the incident RSW. The pressure transducers are separated by an axial distance $\Delta x = x_B - x_A$ so that two different pressure step signals are measured at time t_A, at which the RSW is at location x_A, and at time $t_B = t_A + \Delta t$, namely, when the RSW reaches the second transducer. Signal correlation techniques such as that proposed by Lu & Kim (2000) are then used to compute the wave velocity W which is compared to the local value of the speed of sound c_4 in the initial state 4. If $W > c_4$, then the wave moves at supersonic speed with respect to unperturbed conditions and it is indeed a non-classical RSW. Details of the experimental facility and preliminary results for nitrogen gas are given by Fergason *et al.* (2003).

Preliminary trials using diatomic nitrogen in thermodynamic conditions close to design ones, see Fergason *et al.* (2003), show the non-ideal behaviour of the diaphragm, which opened only partially during all trials. In figure 5(*a*), a typical diaphragm burst is shown, with two opened petals out of four, thus leaving half of the diaphragm as an obstacle to the flow. The resulting flow field is highly three-dimensional and it is studied here by means of numerical simulations. Thompson & Loutrel (1973) discussed the suitability of metal diaphragms in dense gas shock tube experiments. They argued that because of the high acoustic impedance ρc of the fluid, the pressure difference across the diaphragm is rapidly equalized following a small increase δu in the fluid velocity, according to the relation $\delta P = \rho c\, \delta u$, thus resulting in an incomplete petalling of the diaphragm along one or two pre-cut fracture lines. Thompson & Loutrel (1973) suggested using fragile materials such as tempered glass for diaphragms. However,

https://doi.org/10.1017/S0022112007006313 Published online by Cambridge University Press

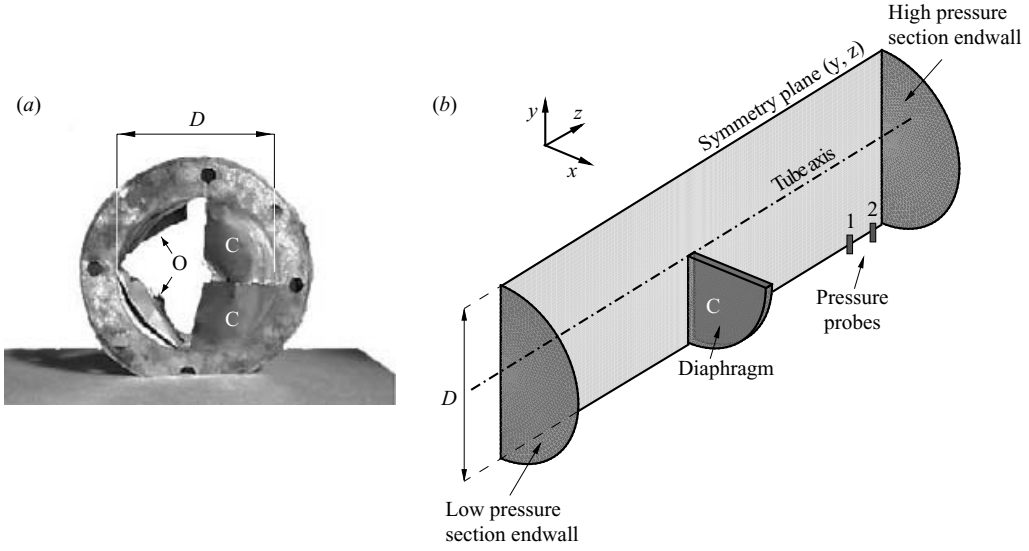

FIGURE 5. (*a*) Partial rupture of the shock tube diaphragm after the experimental trials with nitrogen gas (Fergason *et al.* 2003). D is the tube diameter and the labels O and C indicate opened and unopened diaphragm petals, respectively. (*b*) Geometry of the computational domain (the z-coordinate is not to scale).

diaphragms made of fragile material require the use of a special device to start the diaphragm opening from its centre. Otherwise, a rigid circular membrane that is constrained at its boundary and is subjected to a uniform load starts breaking along its boundary, namely, the diaphragm does not break, but rather detaches from the shock tube wall and moves as a whole towards the low-pressure section endwall. Usually, the trigger device is a simple striker mechanism, which has been deemed here to introduce a significant disturbance in the flow field and possibly to alter the uniformity of the temperature field. Note also that the acoustic impedance of N_2 in the experimental conditions, namely, $\rho c \sim 1.4 \times 10^3\,\mathrm{kg\,m^{-2}s^{-1}}$ at $P = 4.8\,\mathrm{atm}$ and $T = 623$ K (see Fergason *et al.* 2003) is one order of magnitude smaller than the expected value for fluid PP10, for which $\rho c \sim 1.4 \times 10^4\,\mathrm{kg\ m^{-2}s^{-1}}$. Therefore, in the dense gas experiment, the flow closure due to the partial diaphragm opening is expected to be more severe.

Initial conditions for the experiment has been computed by Fergason (2001) and are reported in table 2. The unopened portion of the diaphragm (figure 5*b*), is assumed not to be deformable, and initial conditions are discontinuous across the diaphragm section, therefore, the diaphragm dynamics is not modelled. The fluid thermodynamic properties are computed using the non-polytropic Martin–Hou model and the effects of fluid viscosity and thermal conductivity in the smooth part of the flow field are assumed to be negligible. The symmetry with respect to the (y, z)-plane, z being the axial coordinate, has been enforced and the three-dimensional computational domain represents only half of the shock tube (figure 5*b*).

A grid convergence study is performed to quantify the grid dependency of the computed flow field in general, and of the leading rarefaction shock front in particular. The fact that the grid resolution used in the dilute gas case is sufficient to capture the main flow-field features does not provide any indication for the dense gas computations, since the differences in the local sound speed and hence in the

https://doi.org/10.1017/S0022112007006313 Published online by Cambridge University Press

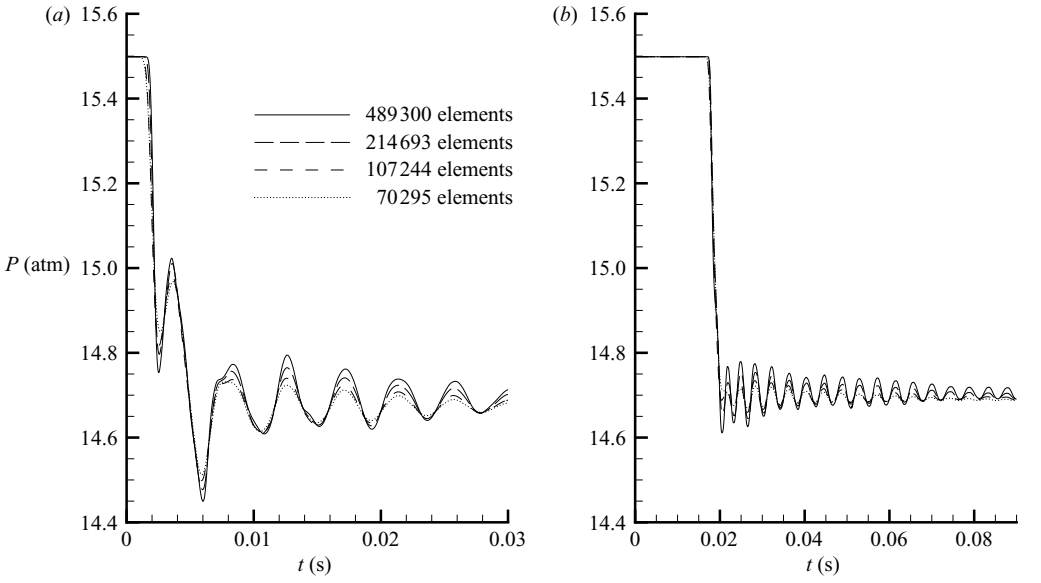

FIGURE 6. Computed pressure profiles at two different stations along the shock tube wall for different grid resolutions. (*a*) Probe 1, located at $z_1 - z_{diaph} = 0.07\,\mathrm{m}$ (1.4D). (*b*) Probe 2, located at $z_2 - z_{diaph} = 1.07\,\mathrm{m}$ (21.4D).

wave speed in the two cases is almost one order of magnitude. Four different grids made of prisms with a triangular base are considered, each totalling 70 925, 107 244, 214 693 and 489 300 elements, respectively. In each grid, the element size in the z-direction is uniform and the node location along each cross-section is kept constant, that is, the grid is obtained by 'extruding' an unstructured grid of triangles from the low-pressure-section endwall to the high-pressure-section endwall. In figure 6, the pressure signals at two different locations (probes 1 and 2) are shown for different grid resolutions. The probe positions are chosen to show a representative signal near the diaphragm location – probe 1 is located 0.07 m or 1.4D from the diaphragm, where multidimensional effects dominate – and near the endwall, where the pressure signal is to be measured during the experiment. For both probes, the main features of the pressure signal are captured already on the coarsest grid, in terms of post-shock average pressure level and of the local frequency of post-shock oscillations. The intensity of post-shock pressure disturbances increases with grid resolution; hence, with respect to this quantity, the results are grid dependent, as is the case for the dilute gas computations in § 4.1.

The peculiarities of the pressure profiles at stations 1 and 2 can be explained by resorting to figures 7–10, where the isopycnics of the flow field along the planes $x = 0\,\mathrm{m}$ and $y = 0\,\mathrm{m}$ are shown at times $t = 0.7857, 1.473, 1.964$ and $2.946\,\mathrm{ms}$, respectively. In all plots, the shaded region represents the $\Gamma > 0$, namely, the classical region, whereas $\Gamma < 0$ elsewhere.

After 0.7857 ms from the diaphragm (instantaneous) opening (figure 7), the flow field presents almost two-dimensional features in the (x, y)-plane, cf. the plot in the $y = 0\,\mathrm{m}$ plane, where isopycnics are almost parallel. The compression shock wave, the contact surface and the rarefaction shock wave are completely formed already. On the upper portion of the flow field, approximately for $y > 0.025\,\mathrm{m} = D/4$, these surfaces of discontinuity are normal to the axis of the shock tube, as is the case

https://doi.org/10.1017/S0022112007006313 Published online by Cambridge University Press

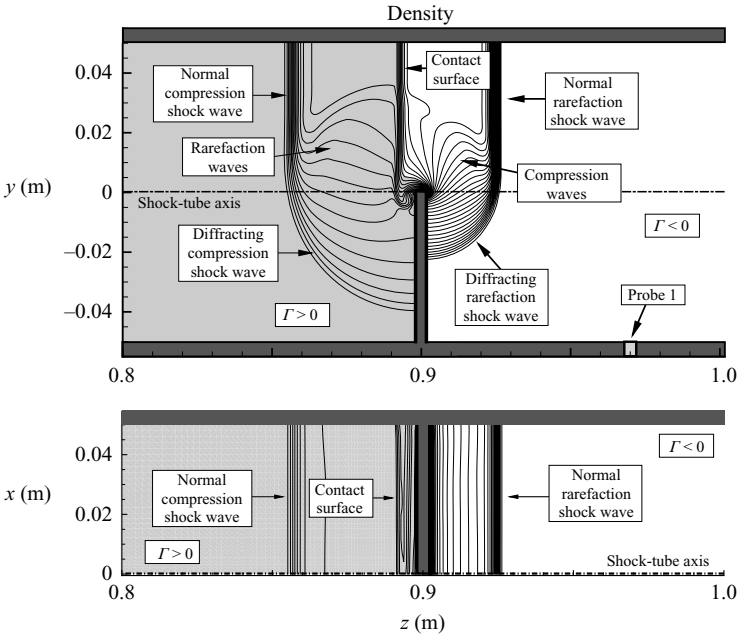

FIGURE 7. Isopycnics at time $t = 0.7857$ ms on the planes (*a*) $x = 0$ m and (*b*) $y = 0$ m for the non-classical shock tube problem. The shaded region indicates the classical $\Gamma > 0$ states.

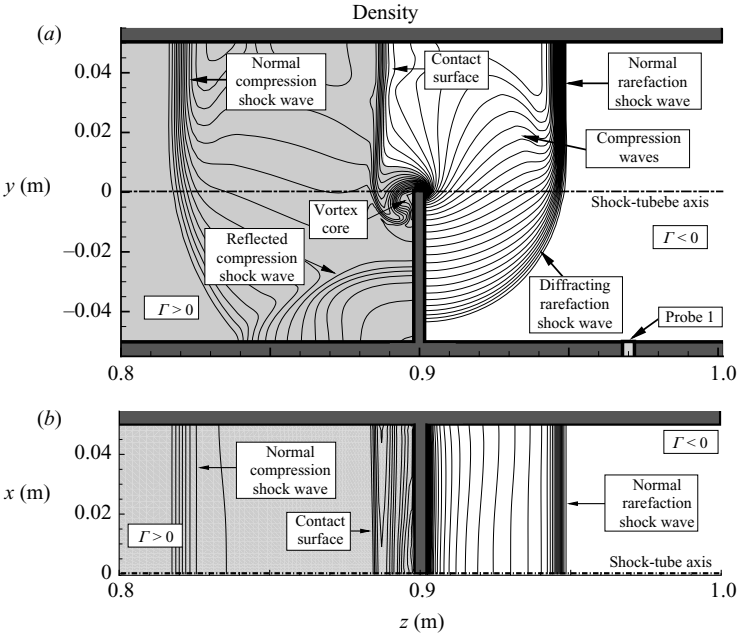

FIGURE 8. As figure 7 but for $t = 1.473$ ms.

for a complete diaphragm burst (one-dimensional flows). Near the diaphragm, both the CSW and the RSW diffract and consequently their intensity is reduced, resulting in rarefaction and compression waves being sent back towards the diaphragm edge from the CSW and the RSW, respectively. Note that the rarefaction and compression

https://doi.org/10.1017/S0022112007006313 Published online by Cambridge University Press

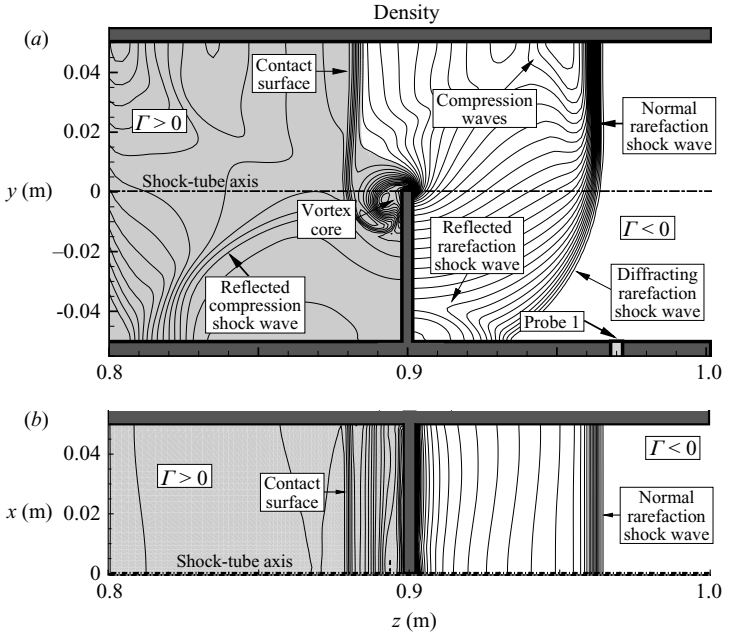

FIGURE 9. As figure 7 but for $t = 1.964$ ms.

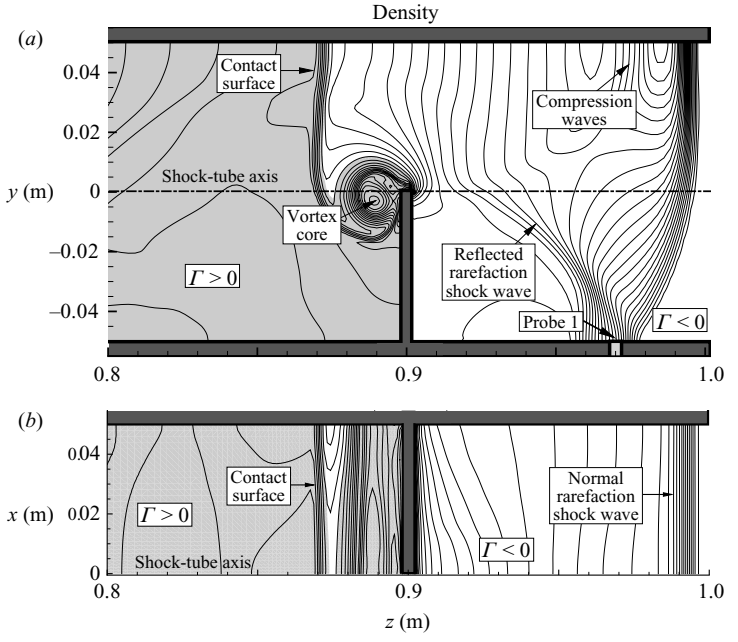

FIGURE 10. As figure 7 but for $t = 2.946$ ms.

waves occur in the classical and non-classical regimes, respectively. In contrast to what was observed by Persico *et al.* (2005) in the case of the diffraction of a classical (isentropic) rarefaction wave, the compression wave past the leading RSW does not coalesce into a compression shock. Instead, since $\Gamma < 0$, it spreads in time as an

https://doi.org/10.1017/S0022112007006313 Published online by Cambridge University Press

isentropic compression wave, a peculiar behaviour of non-classical flows. At time $t = 1.473$ ms (figure 8), the diffracted CSW has been reflected at the tube wall and the reflected wave starts interacting with the vortex shedding from the diaphragm edge. Three-dimensional effects are now evident at the vortex location. The vortex, with axis initially straight and parallel to the x-direction, is generated as a result of flow separation at the diaphragm edge, where the CS rolls up into slip surface (see e.g. Skews 1967; Sun & Takayama 2003). Note that in the present inviscid simulation, flow separation occurs because of the geometry discontinuity at the diaphragm edge. At $t = 1.964$ ms (figure 9), the RSW has already been reflected at the tube wall and the reflected wave propagates towards the high-pressure section. The compression wave resulting from the diffraction of the RSW at the diaphragm edge, cf. time $t = 0.7857$ ms (figure 7), interacts with the upper portion of the tube and is then reflected towards the normal portion of the RSW. The reflected RSW appears more clearly at time $t = 2.946$ ms (figure 10) when the flow field is fully three-dimensional. Compression waves originating at the diaphragm location, cf. time $t = 0.7857$ ms (figure 7), start interacting with the leading RSW on the $y = 0.05$ m wall, thus reducing its intensity. At $y = 0$ m, the shock reflection starts transitioning into a Mach reflection (see Jiang *et al.* 1997) although grid resolution is too poor to show this feature clearly. In all situations, the transition between the classical and non-classical gasdynamic regime always occurs through the CS, as in the (one-dimensional) case of a completely opened diaphragm.

The considerations above led to the following interpretation of the pressure signal in figure 6. The first two expansions at probe 1 are due to the passage of the leading and reflected RSWs, respectively. In particular, the leading shock is followed by a compression wave reaching the probe at $\sim$3 ms, when the pressure starts increasing (figure 10). Post-shock oscillations are due to the system of compression/rarefaction waves reflecting at the tube surface. The second rarefaction wave causes a strong under-pressure with respect to the design post-shock value, which may, in principle, result in crossing the two-phase boundary. Although the simulations predict a single-phase vapour flow in the whole flow field, two-phase flow may possibly occur for different initial conditions or as a results of the unmodelled diaphragm dynamics. It should be noted, however, that such a situation is not critical in that the RSW moves with a higher speed with respect to the local flow velocity at which liquid drops are advected, at most.

Sufficiently far from the diaphragm, i.e. probe 2 in figure 6, the first, strongest, reflected waves coalesce into a single rarefaction shock front normal to the tube axis, as in the one-dimensional case, similarly to what was observed by Chang & Kim (1995) and Jiang *et al.* (1997) in the case of a classical CSW emerging from a shock tube and expanding into a tube with a larger cross-sectional area. From figure 11, the velocity components u and v normal to the tube axis are, in fact, negligible at station 2, i.e. less than 1% of the velocity component w parallel to the axis itself, whereas u and v are about 5% of w close to the diaphragm (probe 1). The resulting planar shock wave is weaker than that theoretically attainable by a complete burst of the shock tube diaphragm. Relevant quantities in the two cases are summarized in table 3. Although the wave speed and hence the Mach number are almost the same, the pressure difference across the RSW resulting from an incomplete burst of the diaphragm is only 81% of its design value, thus making the requirements on the measurement chain more strict (see Fergason *et al.* 2003). Post-shock pressure oscillations are due to the compression/rarefaction wave system past the leading RSW and eventually result in disturbances which are expected to reduce the correlations

https://doi.org/10.1017/S0022112007006313 Published online by Cambridge University Press

	W (m s^{-1})	Mach	ΔP (atm)
Complete burst	31.70	1.017	1.00
Partial burst	31.61	1.014	0.81

TABLE 3. Wave speed W, Mach number and pressure difference across the rarefaction shock wave resulting from a partial and a full burst of the diaphragm for the non-classical shock tube problem.

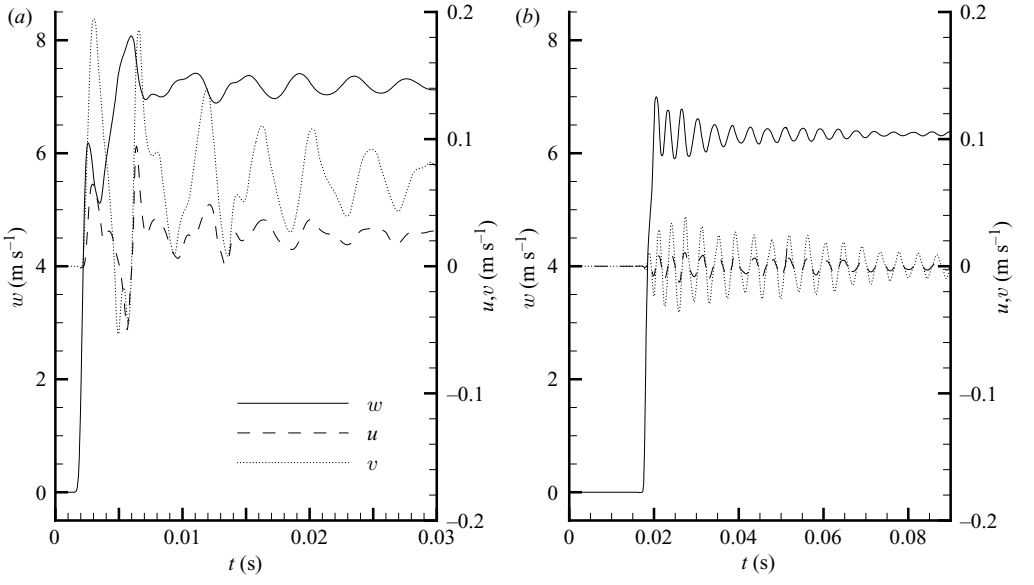

FIGURE 11. Computed velocity profiles at two different stations along the shock tube wall for different grid resolutions. (*a*) Probe 1, located at $z_{diaph} - z_5 = 0.07$ m (1.4D). (*b*) Probe 2, located at $z_{diaph} - z_3 = 1.07$ m (21.4D). The velocity components along the x, y and z axes are indicated by u, v and w, respectively.

between pressure signals and therefore reduce the accuracy of the measurement of the wave speed W.

The triple-discontinuity flow field considered here provides a unique point of view in that it allows us to observe the build-up of a non-classical RSW discussed above together with the classical case of the formation of a classical CSW, the CS being the boundary between the non-classical and classical regimes. Many similarities exist between the present results and those reported by Chang & Kim (1995) and Jiang *et al.* (1997) for a classical CSW expanding into a tube of larger cross-sectional area. In particular, on the low-pressure section of the shock tube, which evolves in the classical regime, the shock propagation and interaction with the vortex shedding from the diaphragm edge (see also Chatterjee 1999) is qualitatively coincident with the phenomena described by these authors. More details have also been observed by Jiang *et al.* (1997), concerning the splitting of the diffracted–reflected shock wave as a result of the interaction with the vortex and the instability of the shear layer, which has been

https://doi.org/10.1017/S0022112007006313 Published online by Cambridge University Press

shown to be a purely inviscid instability, in accordance with the results presented by Blumen, Drazin & Billings (1975) and Drazin & Davey (1977). These flow features are not captured in the present simulations possibly because of the lack of grid resolution. Note, however, that – within the limit of the approximation of considering an instantaneous diaphragm opening – the shock evolution up to the formation of normal shock fronts, in both the low- and high-pressure section is strongly influenced by the mutual interaction of the compression waves generated by the RSW with the CSW and vice versa. In particular, dilute gas simulations show that the resulting shock strength is larger than that predicted by considering the expansion of the CSW and of the rarefaction wave separately. Remarkably enough and differently from the CSW which is the usual object of the experimental investigation, the propagation of the non-classical RSW is not perturbed by the interaction with the CS and is therefore, in some sense, a simpler problem to study.

5. Conclusions

A novel numerical scheme has been presented to simulate three-dimensional non-classical gasdynamic flow fields in the vapour phase using a multiparameter thermodynamic model. The method allows for the use of unstructured hybrid grids made of elements of different types and it is centred around an extension of the Roe linearization technique to a non-ideal thermodynamic model.

The proposed technique has been applied to the simulation of the formation process of a single rarefaction shock front in three-dimensional shock tube flows resulting from the partial burst of the diaphragm. Numerical results indicate that a planar rarefaction shock wave is eventually formed sufficiently far from the diaphragm section, as the initial disturbances coalesce into a single rarefaction shock front. However, pressure disturbances past the shock wave caused by the reflections of a system of compression/rarefaction waves at the tube surface may introduce non-negligible error in the determination of the wave speed, a critical aspect of the experimental strategy. Moreover, the pressure jump across the rarefaction shock wave is predicted to be 19% smaller than that resulting from a complete burst of the diaphragm.

Because of the high acoustic impedance of fluid PP10 at experimental conditions, difficulties due to incomplete diaphragm opening are expected to be even more severe, to such an extent that it can possibly prevent the formation of a rarefaction shock wave; repeatability of the experiment is also expected to decrease. The use of more reliable opening mechanisms, such as, for example, fast opening valves, is therefore suggested for future experimental investigations of non-classical shock tube flows of dense gases.

The author is deeply indebted to Dr Stephen Fergason and to Professor Brian Argrow for invaluable comment and suggestions.

REFERENCES

Argrow, B. M. 1996 Computational analysis of dense gas shock tube flow. *Shock Waves* **6**, 241–248.

Bethe, H. A. 1942 The theory of shock waves for an arbitrary equation of state. *Tech. Rep.* 545. Office of Scientific Research and Development.

Blumen, W., Drazin, P. G. & Billings, D. F. 1975 Shear layer instability of an inviscid compressible fluid. Part 2. *J. Fluid Mech.* **71**, 305–316.

https://doi.org/10.1017/S0022112007006313 Published online by Cambridge University Press

Borisov, A. A., Borisov, Al. A., Kutateladze, S. S. & Nakoryakov, V. E. 1983 Rarefaction shock waves near the critical liquid–vapour point. *J. Fluid Mech.* **126**, 59–73.

Brown, B. P. & Argrow, B. M. 1997 Two-dimensional shock tube flow for dense gases. *J. Fluid Mech.* **349**, 95–115.

Callen, H. B. 1985 *Thermodynamics and an Introduction to Thermostatistics*, 2nd edn. Wiley.

Chang, K.-S. & Kim, J.-K. 1995 Numerical investigation of inviscid shock wave dynamics in an expansion tube. *Shock Waves* **5**, 33–45.

Chatterjee, A. 1999 Shock wave deformation in shock–vortex interactions. *Shock Waves* **9**, 95–105.

Colonna, P. & Silva, P. 2003 Dense gas thermodynamic properties of single and multicomponent fluids for fluid dynamics simulations. *Trans. ASME* I: *J. Fluids Engng* **125**, 414–427.

Cramer, M. S. 1989 Negative nonlinearity in selected fluorocarbons. *Phys. Fluids* **1** (11), 1894–1897.

Cramer, M. S. & Kluwick, A. 1984 On the propagation of waves exhibiting both positive and negative nonlinearity. *J. Fluid Mech.* **142**, 9–37.

Drazin, P. G. & Davey, A. 1977 Shear layer instability of an inviscid compressible fluid. Part 3. *J. Fluid Mech.* **82**, 255–260.

Emanuel, G. 1994 Assessment of the Martin–Hou equation for modelling a nonclassical fluid. *Trans. ASME* I: *J. Fluids Engng* **116**, 883–884.

Fergason, S. H. 2001 Dense gas shock tube: design and analysis. PhD thesis, University of Colorado, Boulder.

Fergason, S. H., Ho, T. L., Argrow, B. M. & Emanuel, G. 2001 Theory for producing a single-phase rarefaction shock wave in a shock tube. *J. Fluid Mech.* **445**, 37–54.

Fergason, S. H., Guardone, A. & Argrow, B. M. 2003 Construction and validation of a dense gas shock tube. *J. Thermophys. Heat Tr* **17**, 326–333.

Glass, I. I. & Sislian, J. P. 1994 *Nonstationary Flows and Shock Waves*. Clarendon.

Godlewski, E. & Raviart, P. A. 1994 *Numerical Approximation of Hyperbolic Systems of Conservation Laws*. Springer.

Guardone, A. 2001 Nonclassical gasdynamics: thermodynamic modeling and numerical simulation of multidimensional flows of BZT fluids. PhD thesis, Politecnico di Milano, Italy.

Guardone, A. & Argrow, B. M. 2005 Nonclassical gasdynamic region of selected fluorocarbons. *Phys. Fluids* **17** (11), 116102–1–17.

Guardone, A. & Vigevano, L. 2002 Roe linearization for the van der Waals gas. *J. Comput. Phys.* **175**, 50–78.

Guardone, A., Vigevano, L. & Argrow, B. M. 2004 Assessment of thermodynamic models for dense gas dynamics. *Phys. Fluids* **16** (11), 3878–3887.

Harten, A. & Hyman, J. M. 1983 Self adjusting grid methods for one-dimensional hyperbolic conservation laws. *J. Comput. Phys.* **50**, 253–269.

Hayes, W. 1960 The basic theory of gasdynamic discontinuities. In *Fundamentals of Gasdynamics* (ed. H. W. Emmons), *High Speed Aerodynamics and Jet Propulsion*, vol. 3, pp. 416–481. Princeton University Press.

Ivanov, A. & Novikov, S. 1961 Rarefaction shock waves in iron and steel. *Sov. Phys. J. Exp. Theor. Phys.* **40**, 1880–1882.

Jiang, Z., Takayama, K., Babinsky, H. & Meguro, T. 1997 Transient shock-wave flows in tubes with a sudden change in cross-section. *Shock Waves* **7**, 151–162.

Lambrakis, K. C. & Thompson, P. A. 1972 Existence of real fluids with a negative fundamental derivative. *Phys. Fluids* **15** (5), 933–935.

van Leer, B. 1974 Towards the ultimate conservative difference scheme II. Monotonicity and conservation combined in a second order scheme. *J. Comput. Phys.* **14**, 361–370.

Lu, F. & Kim, C. H. 2000 Detection of wave propagation by cross correlation, In *38th Aerospace Sciences Meeting and Exhibit, Reno, NV*, paper 2000-0676.

Martin, J. J. & Hou, Y. 1955 Development of an equation of state for gases. *AIChE J.* **1**, 142–151.

Martin, J. J., Kapoor, R. M. & De Nevers, N. 1958 An improved equation of state. *AIChE J.* **5**, 159–160.

Menikoff, R. & Plohr, B. J. 1989 The Riemann problem for fluid flow of real material. *Rev. Mod. Phys.* **61**, 75–130.

Perry, R. H. & Green, D. 1984 *Perry's Chemical Engineers' Handbook*, 6th edn. McGraw–Hill.

https://doi.org/10.1017/S0022112007006313 Published online by Cambridge University Press

Persico, G., Gaetani, P. & Guardone, A. 2005 Dynamic calibration of fast-response probes in low-pressure shock tubes. *Meas. Sci. Technol.* **16**, 1751–1759.

Petrie-Repar, P. & Jacobs, P. A. 1998 A computational study of shock speeds in high-performance shock tubes. *Shock Waves* **8**, 79–91.

Rider, W. J. & Bates, J. W. 2001 A high-resolution Godunov method for modeling anomalous fluid behaviour. In *Godunov Methods: Theory and Application.* (ed. E. F. Toro). Kluwer/Plenum Academic.

Roe, P. L. 1981 Approximate Riemann solvers, parameter vectors, and difference schemes. *J. Comput. Phys.* **43**, 357–372.

Selmin, V. 1993 The node-centred finite volume approach: bridge between finite differences and finite elements. *Comput. Meths. Appl. Mech. Engng* **102**, 107–138.

Shu, C.-W. 1988 Total-variation-diminishing time discretizations. *SIAM J. Sci. Stat. Comput.* **9**, 1073–1084.

Skews, B. 1967 The shape of a diffracting shock wave. *J. Fluid Mech.* **29**, 297–304.

Sun, M. & Takayama, K. 2003 Vorticity production in shock diffraction. *J. Fluid Mech.* **478**, 237–256.

Thompson, P. A. 1971 A fundamental derivative in gas dynamics. *Phys. Fluids* **14**, 1843–1849.

Thompson, P. A. & Lambrakis, K. C. 1973 Negative shock waves. *J. Fluid Mech.* **60**, 187–208.

Thompson, P. A. & Loutrel, W. F. 1973 Opening time of brittle shock-tube diaphragms for dense fluids. *Rev. Sci. Instrum.* **44**, 1436–1437.

Thompson, P. A., Carofano, G. A. & Kim, Y. 1986 Shock waves and phase changes in a large heat capacity fluid emerging from a tube. *J. Fluid Mech.* **166**, 57–96.

Weyl, H. 1949 Shock waves in arbitrary fluids. *Commun. Pure Appl. Maths.* **2**, 102–122.

Zamfirescu, C., Guardone, A. & Colonna, P. 2006 Preliminary design of the FAST dense gas Ludwieg tube. *AIAA Paper*. 2006–3249.

Zel'dovich, Y. B. 1946 On the possibility of rarefaction shock waves. *Sov. Phys., J. Exp. Theor.* **4**, 363–364.

https://doi.org/10.1017/S0022112007006313 Published online by Cambridge University Press